

Influence of sputtering ambient with hydrogen gas on optoelectrical properties of Ta-doped tin oxide

Haozhen Li(李昊臻), Xingqian Chen(陈兴谦), Minqiu Du(杜敏求), Wei Chen(陈伟), and Xiaolong Du(杜小龙)
Citation: Chin. Phys. B, 2025, 34 (**7**): 077303. DOI: 10.1088/1674-1056/adc97f
http://cpb.iphy.ac.cn; http://iopscience.iop.org/cpb

What follows is a list of articles you may be interested in

Role of self-assembled molecules' anchoring groups for surface defect passivation and dipole modulation in inverted perovskite solar cells

Xiaoyu Wang(王啸宇), Muhammad Faizan, Kun Zhou(周琨), Xinjiang Wang(王新江), Yuhao Fu(付钰豪), and Lijun Zhang(张立军)
Chin. Phys. B, 2024, 33 (**10**): 107303. DOI: 10.1088/1674-1056/ad711f

Delayed response to the photovoltaic performance in a double quantum dots photocell with spatially correlated fluctuation

Sheng-Nan Zhu(祝胜男), Shun-Cai Zhao(赵顺才), Lu-Xin Xu(许路昕), and Lin-Jie Chen(陈林杰)
Chin. Phys. B, 2023, 32 (**5**): 057302. DOI: 10.1088/1674-1056/ac8e97

Effects of preparation parameters on growth and properties of β-Ga_2O_3 film

Zi-Hao Chen(陈子豪), Yong-Sheng Wang(王永胜), Ning Zhang(张宁), Bin Zhou(周兵), Jie Gao(高洁), Yan-Xia Wu(吴艳霞), Yong Ma(马永), Hong-Jun Hei(黑鸿君), Yan-Yan Shen(申艳艳), Zhi-Yong He(贺志勇), and Sheng-Wang Yu(于盛旺)
Chin. Phys. B, 2023, 32 (**1**): 017301. DOI: 10.1088/1674-1056/ac728c

Effects of post-annealing on crystalline and transport properties of Bi_2Te_3 thin films

Qi-Xun Guo(郭奇勋), Zhong-Xu Ren(任中旭), Yi-Ya Huang(黄意雅), Zhi-Chao Zheng(郑志超), Xue-Min Wang(王学敏), Wei He(何为), Zhen-Dong Zhu(朱振东), and Jiao Teng(滕蛟)
Chin. Phys. B, 2021, 30 (**6**): 067307. DOI: 10.1088/1674-1056/abee6c

Effects of rapid thermal annealing on crystallinity and Sn surface segregation of $Ge_{1-x}Sn_x$ films on Si (100) and Si (111)

Yuan-Hao Miao(苗渊浩), Hui-Yong Hu(胡辉勇), Jian-Jun Song(宋建军), Rong-Xi Xuan(宣荣喜), He-Ming Zhang(张鹤鸣)
Chin. Phys. B, 2017, 26 (**12**): 127306. DOI: 10.1088/1674-1056/26/12/127306

Influence of sputtering ambient with hydrogen gas on optoelectrical properties of Ta-doped tin oxide

Haozhen Li(李昊臻)[1,2,4], Xingqian Chen(陈兴谦)[1,2,4], Minqiu Du(杜敏求)[1,4], Wei Chen(陈伟)[2,3,†], and Xiaolong Du(杜小龙)[1,2,3,‡]

[1] *Beijing National Laboratory for Condensed Matter Physics, Institute of Physics, Chinese Academy of Sciences, Beijing* 100190, *China*
[2] *Songshan Lake Materials Laboratory, Dongguan* 523808, *China*
[3] *Guangdong SinoPrime Technology Co. Ltd., Dongguan* 523808, *China*
[4] *School of Physical Sciences, University of Chinese Academy of Sciences, Beijing* 100049, *China*

(Received 19 February 2025; revised manuscript received 2 April 2025; accepted manuscript online 7 April 2025)

Ta-doped SnO_2 (TTO) is a suitable candidate to replace transparent conductive oxide (TCO) composed of expensive indium used for optoelectronics and silicon heterojunction solar cells fabricated below 200 °C. However, TTO films fabricated by sputtering at low temperature still demonstrate too high resistance and optical absorptance for application in industry. In this study, we investigate the influence of sputtering ambient on the optoelectrical properties of TTO films. The addition of hydrogen and oxygen to argon during sputtering leads to a large improvement in the optoelectrical properties of TTO films. The best TTO film has a low average absorptance of 1.9% and a low resistance of 3.8×10^{-3} Ω·cm with a high carrier density of 9.3×10^{19} cm^{-3} and mobility of 17.8 $cm^2 \cdot V^{-1} \cdot s^{-1}$. The microstructural and compositional properties of TTO films were characterized using x-ray diffraction, x-ray photoelectron spectroscopy and UV–Vis spectrophotometry. A proper ratio of hydrogen to oxygen in the sputtering gas improves the crystallinity and the doping efficiency of Ta. Optical absorptance is also reduced with suppressed formation of Sn(II) in the TTO films. Therefore, our findings exhibit remarkable potential for the industrial application of TTO as a low-cost TCO.

Keywords: transparent conductive oxide (TCO), magnetron sputtering, ambient, Ta-doped SnO_2, H_2

PACS: 73.61.–r, 78.66.–w, 01.50.ff, 68.35.bg

DOI: 10.1088/1674-1056/adc97f **CSTR:** 32038.14.CPB.adc97f

1. Introduction

Transparent conductive oxides (TCOs) fabricated in processes below 200 °C play a vital role in low-temperature optoelectronic applications, including thin-film transistors, silicon heterojunction (SHJ) solar cells, etc.[1,2] Heavily doped wide-bandgap oxide semiconductors, such as In_2O_3, ZnO and SnO_2, have served as conventional transparent electrode materials for decades.[3] These materials exhibit exceptional electrical conductivity attributed to Fermi level shifting into the conduction band, leading to high free-carrier concentrations. The wide band gap effectively suppresses interband transitions in the visible spectrum due to their high energy requirements, resulting in excellent optical transparency. These superior optoelectronic characteristics establish doped In_2O_3 as the predominant TCO material in practical applications.[4,5] However, the limited natural abundance of indium combined with elevated production costs makes In_2O_3-based TCOs a key cost-reduction challenge in large-scale industrial manufacturing.

Doped ZnO has emerged as a prominent alternative TCO material offering significant cost advantages.[6] Nevertheless, the strong ionic character of zinc renders ZnO insufficiently stable for corrosive back-end processes. Consequently, SnO_2 thin films are gaining substantial research interest due to their desirable optoelectronic performance and enhanced chemical stability.[7]

SnO_2 films are typically deposited via physical vapor deposition (PVD), chemical vapor deposition (CVD) or alternative techniques.[8] Film characteristics are governed by crystallization quality, defect states and impurity incorporation. Among them, magnetron sputtering growth is an efficient and economical PVD technique for low-temperature thin-film growth. Intrinsic SnO_x has achieved notable advancements in heterojunction solar cells,[9] yet its exceptional optoelectronic properties remain insufficiently investigated. Other SnO_2-based doped TCO materials, however, have been extensively explored as well.[10] F-doped SnO_2 (FTO) demonstrates high quality when fabricated using high-temperature spray pyrolysis, but suffers from intrinsic self-compensation defects at interstitial positions under heavy F doping.[11] Sb-doped SnO_2 (ATO) has garnered attention for its high carrier concentration, though Sb doping induces conduction band minimum (CBM) bending that elevates carrier effective mass and constrains maximum theoretical mobility,[12] as experimentally

†Corresponding author. E-mail: wchen@sslab.org.cn
‡Corresponding author. E-mail: xldu@iphy.ac.cn

© 2025 Chinese Physical Society and IOP Publishing Ltd. All rights, including for text and data mining, AI training, and similar technologies, are reserved.

verified.[13]

Ta(V) (ionic radius: 69 pm) exhibits near-identical dimensions to Sn(IV) (71 pm), enabling minimal lattice strain in SnO_2 while maintaining effective donor behavior. Resonant Ta doping has been theoretically demonstrated to reduce hybridization between the CBM and dopant states through its 5d orbital characteristics, resulting in reduced carrier effective mass (via *ab initio* density functional theory calculations) and enhanced mobility exceeding 25 $cm^2 \cdot V^{-1} \cdot s^{-1}$, superior to Sb-doped SnO_2 (ATO) in experimental comparisons.[13] High-performance Ta-doped SnO_2 (TTO) films with resistivity $< 10^{-3}$ Ω·cm can be fabricated via magnetron sputtering,[14] pulsed laser deposition,[15] and sol–gel spin coating.[16] Notably, sputtered TTO films achieved record-low resistivity (5.4×10^{-2} Ω·cm), though requiring high-temperature processing (600 °C) that precludes low-temperature industrial applications.[17]

In this study, we aim to optimize the optoelectronic properties of TTO films using RF magnetron sputtering under controlled atmospheric conditions below 200 °C. The deposition atmosphere critically influences film microstructure through chemical bonding configurations and defect formation mechanisms,[18,19] both of which govern electronic properties. In SnO_x systems, the coexistence of Sn(IV) and Sn(II) oxidation states, modulated by oxygen activity, directly impacts defect chemistry and electronic structure.[20] Rutile-phase SnO_2 (band gap $\sim$ 3.8 eV) dominates high-performance TCOs, outperforming SnO in both optical transparency and electrical conductivity,[8] highlighting the need to suppress Sn(II) formation during growth.

Hydrogen incorporation during sputtering exerts dual functionality in tin oxide systems, acting as a donor species while simultaneously modifying crystallinity and chemical bonding.[21] Despite its critical influence, the detailed investigation of H effects on modulating TTO microstructure and optoelectronic properties unfortunately remains very limited. To address this significant issue, we systematically introduced O_2 and/or H_2 into the sputtering environment to elucidate atmospheric effects. Our findings reveal that hydrogen acts as a surfactant, enhancing TTO crystallinity and Ta doping efficiency. Synergistically with oxygen, H effectively suppresses Sn(II) formation, thereby reducing optical absorption centered at $\sim$ 500 nm. These advancements endow TTO films with exceptional optoelectronic performance, positioning them as cost-effective TCO candidates for low-temperature applications.

2. Experimental methods

2.1. Sample preparation

All samples studied in this paper are named TTO:O_xH_y, where x and y represent original high-purity O_2 and H_2 partial pressures, P_O and P_H ($\times 10^{-3}$ Pa), before 7.6×10^{-2} Pa Ar mixes in the growth chamber measured with an ionization gauge. The base pressure is about 4×10^{-4} Pa. The gate valve of the vacuum system was adjusted to change the gas pressure for initial discharge and normal growth. The TTO films were prepared in a homemade RF magnetron sputtering system using a 2 inch hot-pressed SnO_2 target that was doped with 4.12 wt.% Ta_2O_5. An RF power density of 153 mW·cm^{-2}, a growth temperature of 180 °C and a working pressure of 0.4 Pa were chosen as the growth parameters for all samples that were grown on 30 mm × 30 mm glass substrates cleaned beforehand with ethanol, acetone and deionized water each for 20 min in a home-made sputtering system. After sputtering for 28 min, the mass flow controllers for O_2 and H_2 were closed, and each sample was annealed *in situ* at the same temperature in argon ambient for 20 min to release possible bubbles of H_2 or O_2 as well as surplus H from the films.

2.2. Film characterization

The thicknesses of TTO films were determined using a HITACHI Regulus 8100 field-emission scanning electron microscope (SEM). Transmittance and reflectance spectra were obtained using a HITACHI UH4150 UV-Vis spectrophotometer at a wavelength range between 240 nm and 1500 nm, while the Hall measurement was performed with an Ecopia HMS 3000 system to obtain the carrier concentration, mobility and resistivity at room temperature. A Bruker D8-ADVANCE x-ray diffractometer (XRD) with Cu $K\alpha$ radiation was used to acquire the crystallinity and structural properties. Thermo Fisher ESCALAB XI+ x-ray photoelectron spectroscopy (XPS) with Al $K\alpha$ radiation was applied to evaluate the chemical status and relative content.

3. Results and discussion

3.1. The effect of O_2 or H_2 on film properties

In order to explore how ambient affects the performance of TTO films, two samples, TTO:O_1H_0 and TTO:O_0H_1, were individually prepared by adding O_2 or H_2 into Ar atmosphere during sputtering. The partial gas pressures of oxygen and hydrogen (P_O, P_H) are listed in Table 1 together with their optoelectrical properties. The thicknesses D were obtained by SEM. For comparison, sample TTO:O_0H_0 was also listed, which was sputtered with argon only. The Hall effect measurement system and UV-Vis spectrometer were used to evaluate the optical and electrical performance of TTO films, obtaining the resistivity (ρ), carrier concentration (n_e), mobility (μ) and average transmittance (T_{avg}) of films, as shown in Table 1. T_{avg} is calculated from the transmittance spectra shown in Fig. 1(a) according to

$$T_{avg} = \frac{\int \Phi(\lambda)\, T(\lambda)\, d\lambda}{\int \Phi(\lambda)\, d\lambda}, \tag{1}$$

where $\Phi(\lambda)$ is AM1.5G spectral irradiance and the wavelength range of integration is from 400 nm to 1200 nm. It should be noted that the reflectance spectrum, as shown in Fig. 1(a), has a strong impact on the transmittance spectrum of the films. Furthermore, the reflection spectrum strongly depends on film thickness while it acts as the anti-reflection layer. Consequently, the reflection minimum shifts with varying thickness. To minimize thickness dependence and better evaluate optical properties, we analyze absorption (A) rather than transmittance, which is calculated as follows:

$$A(\lambda) = 1 - T(\lambda) - R(\lambda). \tag{2}$$

Herein, A_{avg} represents the parasitic absorption of the film, i.e., lower A_{avg} implies higher effective transmittance. A_{avg} is similarly determined following the same methodology as T_{avg} and the results are presented in Table 1. As shown in Table 1, TTO:O_1H_0 fabricated in ambient with oxygen has a lower A_{avg} (1.7%) than that of TTO:O_0H_0, while the A_{avg} of TTO:O_0H_1 is the highest.

The absorption spectra in logarithmic coordinate of all three samples are plotted in Fig. 1(b). There are two main related absorption ranges with defects at short-wavelength range and free-carrier absorption at long-wavelength range, respectively. In the short-wavelength range from 400 nm to 600 nm, TTO:O_0H_1 has the highest absorption, while the absorption of sample TTO:O_1H_0 is the lowest. It is well known that oxygen vacancy (V_O) in SnO_2 is a ubiquitous deep-level defect and has different photoluminescence peaks at $\sim$ 430 nm and $\sim$ 501 nm.[22] TTO:O_0H_0 was grown under oxygen-poor conditions resulting in the formation of V_O in the film. Furthermore, the Ar + H_2 ambient makes oxygen scarcer due to the reaction of H with O. This leads to the formation of higher concentration of V_O in TTO:O_0H_1. The introduction of oxygen during sputtering suppressed V_O formation, thereby eliminating the $\sim$ 500 nm absorption in TTO:O_1H_0. Meanwhile, the free-carrier absorption in degenerate TCOs dominates the long-wavelength absorption, further explaining the minimal absorption of TTO:O_1H_0 due to its lowest carrier concentration. Surprisingly, TTO:O_0H_1 exhibits lower long-wave absorption than TTO:O_0H_0 despite its higher carrier density, potentially due to hydrogen-induced conduction band modification, which should be further investigated.

Table 1. Fabricating parameters and optoelectrical results of TTO films fabricated under different atmospheres: O_2 + Ar (TTO:O_1H_0), H_2 + Ar (TTO:O_0H_1) and pure Ar (TTO:O_0H_0) as reference.

Sample	P_O (10^{-3} Pa)	P_H (10^{-3} Pa)	T_{avg} (%)	A_{avg} (%)	ρ (10^{-3} Ω·cm)	n_e (10^{19} cm^{-3})	μ (cm^2·V^{-1}·s^{-1})	D (nm)
TTO:O_0H_0	0	0	80.2	2.9	7.9	6.1	12.9	109
TTO:O_1H_0	1	0	77.9	1.7	56.7	0.8	13.0	82
TTO:O_0H_1	0	1	79.8	3.8	9.5	6.5	10.1	120

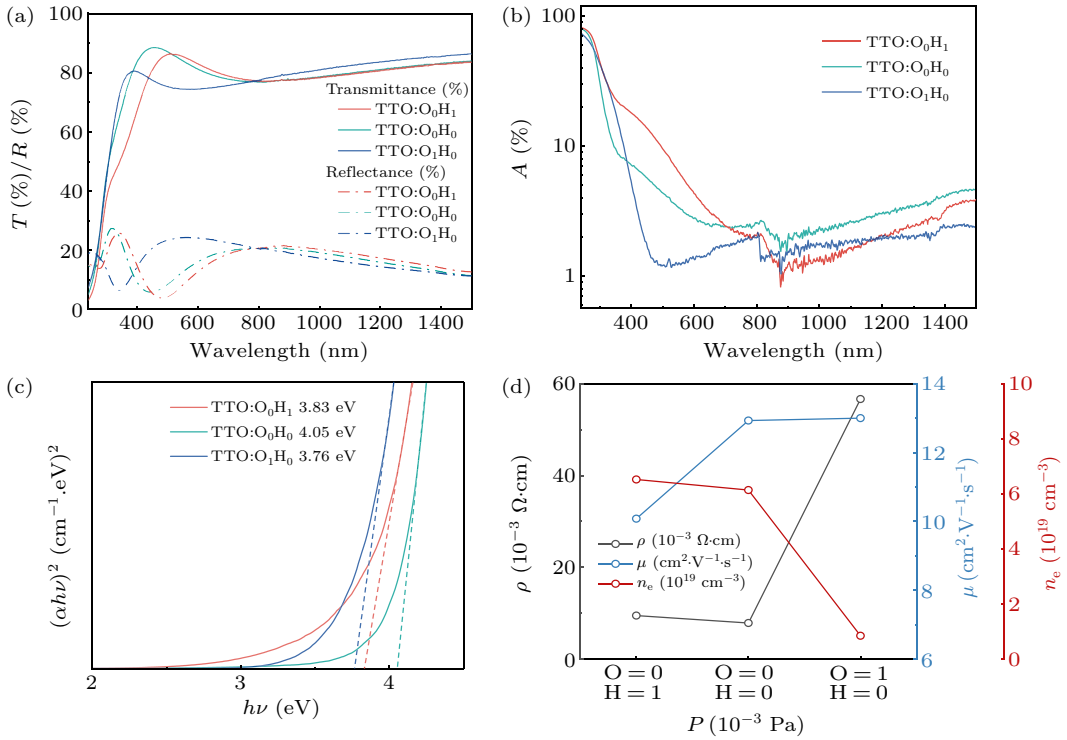


Fig. 1. Optical and electrical properties of TTO films deposited under different atmospheres: O_2 + Ar (TTO:O_1H_0), H_2 + Ar (TTO:O_0H_1), and pure Ar (TTO:O_0H_0) as reference. (a) Optical transmittance (T) spectra represented by a solid line and reflectance (R) spectra by a dashed line; (b) optical absorption (A) spectra; (c) Tauc plots and fitted optical energy gap and (d) resistivities (ρ) in black, mobilities (μ) in blue and carrier concentrations (n_e) in red, obtained by Hall measurement with guidelines.

A Tauc plot is shown in Fig. 1(c) to investigate the optical band gap (E_{opt}) of these samples determined by

$$(\alpha h\nu)^2 = C\left(h\nu - E_{opt}\right), \tag{3}$$

where α is the absorption coefficient calculated from[23]

$$\alpha = \frac{1}{D}\ln\frac{100 - R(\nu)}{T(\nu)}, \tag{4}$$

where D is the film thickness, C is a constant and $h\nu$ is the photon energy. TTO:O_1H_0 has the narrowest optical band gap at 3.76 eV identical to intrinsic SnO_2 at $\sim$ 3.8 eV.[24] This can be ascribed to its low free-carrier concentration (8.5×10^{18} cm^{-3}), which is still not enough for transformation into degenerate semiconductor. The other two samples sputtered without oxygen have higher carrier densities resulting partially from the higher concentration of V_O, which is a donor in SnO_2.[25] They have wider optical band gaps than those of TTO:O_1H_0 due to the Burstein–Moss shift.

For the electrical performance of n-type TCOs, it is known that the resistivity is calculated as follows:

$$\rho = \frac{1}{n_e q \mu}, \tag{5}$$

where q is the carrier charge constant. TTO films deposited in pure argon (TTO:O_0H_0) or argon-hydrogen mixtures (TTO:O_0H_1) demonstrate low resistivity (7.9×10^{-3} Ω·cm and 9.5×10^{-3} Ω·cm) and elevated carrier density. On the other hand, TTO film grown in Ar mixed with O_2 has much higher resistivity (5.7×10^{-2} Ω·cm) with a low concentration below 10^{19} cm^{-3}. Figure 1(d) reveals that neither oxygen nor hydrogen alone in the argon sputtering atmosphere achieves optimal optoelectrical performance.

XPS characterization and fitting were performed on these samples to investigate the electronic states of Sn in SnO_2, as shown in Fig. 2(a). Tin oxides exhibit distinct stoichiometric states: Sn(IV) in SnO_2 and Sn(II) in SnO. Oxygen deficiency promotes SnO formation in SnO_x ($x < 2$), reducing the optical band gap and transparency.[26] Thus, Sn(II) content critically determines the TCO performance of SnO_x. Here, we test the content of Sn(II) by peak fitting of Sn $3d_{5/2}$ and Sn $3d_{3/2}$ in the XPS spectra, as shown in Fig. 2(a), where the peak positions are located at $\sim$ 486 eV and 495 eV, respectively.[27] Each peak profile has a contribution from Sn(IV) and Sn(II) with a binding energy difference of 0.7 eV. Deconvolution of the Sn $3d_{5/2}$ peak ($\sim$ 486 eV) reveals two components: Sn $3d_{5/2}$ (IV) at 486.8 eV (blue) and Sn $3d_{5/2}$ (II) at 486.1 eV (red), as shown in Fig. 2(a). The Sn(II) content of Sn can be estimated semiquantitatively by the ratio of the red peak area to the total area of the blue and red peaks. Figure 2(a) clearly shows that TTO:O_0H_1 has the highest ratio among all three samples, indicating the highest Sn(II) content. The addition of hydrogen to sputtering gas raised the Sn(II) content of Sn in TTO film. The high content of Sn(II) also contributes to the severe absorption of TTO:O_0H_1 at short-wavelength range, forming a broad peak in the absorption spectrum in Fig. 1(b). Conversely, TTO:O_1H_0 shows minimal red peak intensity, indicating low Sn(II) content. O_2 addition to the Ar gas reduces the formation of Sn(II) as well as V_O, reducing short-wavelength absorption.

XRD is performed to investigate the film microstructures in different ambient [Fig. 2(b)]. TTO films grown under hypoxic conditions (TTO:O_0H_0 and TTO:O_0H_1) are prone to form polycrystal with a main XRD peak of rutile SnO_2 (101). Meanwhile, the addition of H_2 turns rutile SnO_2 (211) in TTO:O_0H_0 into (112) in TTO:O_0H_1. In contrast, TTO film sputtered in argon with oxygen shows an amorphous structure. Oxygen incorporation was found to inhibit the growth of (101) as well as other orientations. No peaks involving Ta were observed, implying that there is no phase separation related to Ta. In general, TTO films deposited in argon with either oxygen or hydrogen alone exhibit insufficient optoelectrical properties for device applications. Optimal performance requires balancing optical transparency and electrical conductivity in TTO films.

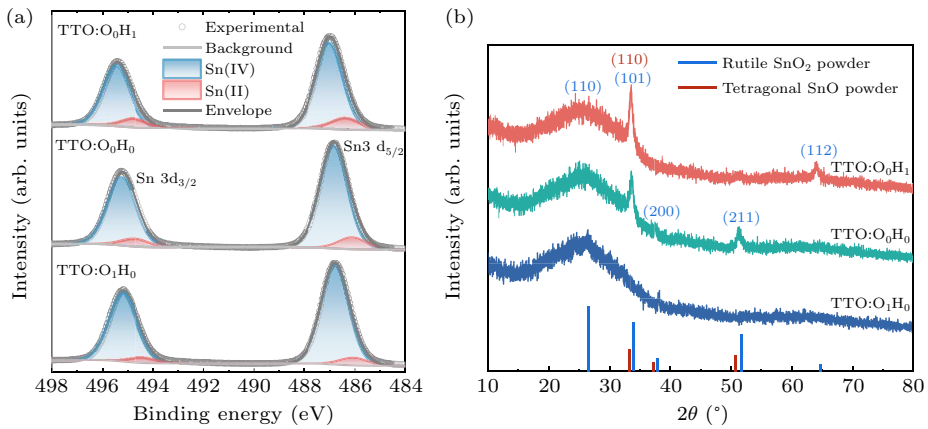


Fig. 2. Sn content and structure of TTO films deposited under different atmospheres: $O_2 + Ar$ (TTO:O_1H_0), $H_2 + Ar$ (TTO:O_0H_1), and pure Ar (TTO:O_0H_0) as reference. (a) XPS spectra of the Sn 3d core level measured after argon plasma sputtering to remove surface contamination and (b) XRD patterns.

3.2. Inlet of H_2 and O_2 for the balanced optoelectrical properties of TTO film

To further explore the influence of H_2 in ambient on TTO films, we varied hydrogen concentration with a fixed pressure of oxygen simultaneously in the sputtering system. The growth parameters and optoelectrical properties are summarized in Table 2 and the trends of the electrical performance are illustrated in Fig. 3(a).

Table 2. Fabrication parameters and optoelectronic properties of TTO films deposited under constant oxygen partial pressure (P_O) and varying hydrogen partial pressure (P_H).

Sample	P_O (10^{-3} Pa)	P_H (10^{-3} Pa)	ρ (10^{-3} Ω·cm)	n_e (10^{19} cm^{-3})	μ (cm^2·V^{-1}·s^{-1})	T_{avg} (%)	A_{avg} (%)	D (nm)
TTO:O_1H_0	1	0	56.7	0.8	13.0	78.3	1.7	88
TTO:$O_1H_{0.5}$	1	0.5	1317.1	0.2	2.5	78.5	1.6	96
TTO:O_1H_1	1	1	521.6	0.3	3.5	78.7	1.4	96
TTO:$O_1H_{1.5}$	1	1.5	4.1	8.2	18.7	79.7	2.1	100
TTO:O_1H_2	1	2	3.8	9.4	17.8	80.6	1.9	101
TTO:O_1H_3	1	3	6.1	6.9	14.7	79.8	2.1	99
TTO:O_1H_5	1	5	–	–	–	75.4	3.2	99

Note: Hall measurement for TTO:O_1H_5 exceeded instrument detection limits.

In comparison to TTO:O_1H_0, the film resistivity of sample TTO:$O_1H_{0.5}$ increases singularly to 1.3 Ω·cm when H_2 is introduced with a partial gas pressure of 5×10^{-4} Pa ($y = 0.5$). The resistivity, however, decreases dramatically to 4.1×10^{-3} Ω·cm when $y = 1.5$ and reaches a minimum of 3.8×10^{-3} Ω·cm at $y = 2$ with large mobility. The film resistivity increases when y increases further, ultimately reaching insulation at $y = 5$. The unchanged P_O for all these samples indicates that the change in sample conductivity originates from the variation of P_H. Hydrogen plays a negative role in the electrical properties of TTO at both stages of small ($y = 0.5$ and 1) and excessive H ($y > 3$), whereas it plays a beneficial role when a moderate amount is introduced.

On the other hand, the change in the average absorption A_{avg} is monotonous, which is almost leveled when y increases from 0 to 1.0 followed by a slight rise when $y = 1.5$, 2 and 3. It displays quite a large increase when $y = 5$.

It is known that hydrogen is a shallow donor in SnO_2 film.[21] How a small amount of H is incorporated and unusually reduces the film conductivity remains unknown. This requires more refined and microscopic studies. We postulate that the combination with oxygen must simultaneously affect the solid structure inside the film and the doping behavior of Ta. However, a proper amount of hydrogen and oxygen enables balanced optoelectrical properties in TTO films, as demonstrated by the high-performance TTO:O_1H_2. The film not only has a very low resistivity resulting from the high carrier concentration of 9.4×10^{19} cm^{-3} and the high mobility of 17.8 cm^2·V^{-1}·s^{-1}, but also a high transmittance of 80.6% due to the low average absorption of 1.9%.

XRD and XPS analyses were conducted to examine hydrogen's influence on film microstructure. The XRD patterns reveal a distinct amorphous-to-polycrystalline transition as y increases from 0 to 0.5 [Fig. 3(b)], indicating enhanced crystallinity. It is well known that hydrogen plays a role as a surfactant during oxide growth by absorbing on the surface and changing the growth mode, which is very sensitive to the growth kinetics. Our results reveal different distribution of the grain orientations in the film when hydrogen is introduced with or without oxygen simultaneously. For the latter, the XRD peak of (101) is dominant with a weak peak of (112) [Fig. 2(b)]. Remarkably, oxygen co-introduction eliminates these peaks, but induces (110), (200) and (211) orientations. Furthermore, the (211) peak intensifies with increasing hydrogen content up to $y = 3$. The film resistivity decreases as y changes from 0.5 to 2. The film with optimal conductive properties has the highest carrier concentration, large mobility as well as the strongest XRD peak of (211) among all samples when y becomes 2. It has been reported that TTO samples grown on glass with stronger (211) and suppressed (101) peaks have better electrical properties,[28,29] which is consistent with our results. As can be seen from the XPS Sn 3d results in Fig. 3(c), there is no obvious increase in the Sn(II) content when y increases from 0 to 2. However, the small number of hydrogen-involved samples (TTO:$O_1H_{0.5}$ and TTO:O_1H_1) with similar XRD profiles show minimal structural variations, and the available data do not directly explain their extremely deteriorated electrical properties, which need to be further investigated. When the hydrogen amount increases further in the sputtering system, an XRD peak appears near 33.5°, which can be ascribed to the formation of tetragonal SnO (110) in the film. When y increases from 2 to 5, the intensity of SnO (110) increases, while all other XRD peaks related to rutile SnO_2 weaken and finally disappear when $y = 5$. Excessive hydrogen introduction elevates film resistivity and average absorption, demonstrating hydrogen's detrimental effects at high concentrations. Sample TTO:O_1H_5 becomes insulating and dark in color. Its transparency is also largely reduced. XPS analysis in Fig. 3(c) confirms substantial Sn(II) formation under these conditions, indicating a highly reductive growth environment. Excessive Sn(II) aggregation leads to the formation of SnO. The abundant SnO phases act as scattering and recombination

centers in TTO, significantly suppressing both carrier mobility and concentration.

Optical band gaps of TTO films are obtained by the Tauc plot shown in Fig. 3(d). The amorphous TTO:O_1H_0 has a low band gap (3.76 eV) in comparison to the polycrystalline ones (3.86 eV of TTO:$O_1H_{0.5}$ and 3.84 eV of TTO:O_1H_1). When y reaches 1.5 or higher, the band gap of the TTO films widens due to the Burstein–Moss effect of high carrier densities. When excess H_2 is introduced into the ambient, E_{opt} of the TTO:O_1H_5 decreases significantly, suggesting that a mixture of amorphous SnO_2 and tetragonal SnO has a much lower band gap of 2.5 eV–3.0 eV.[30]

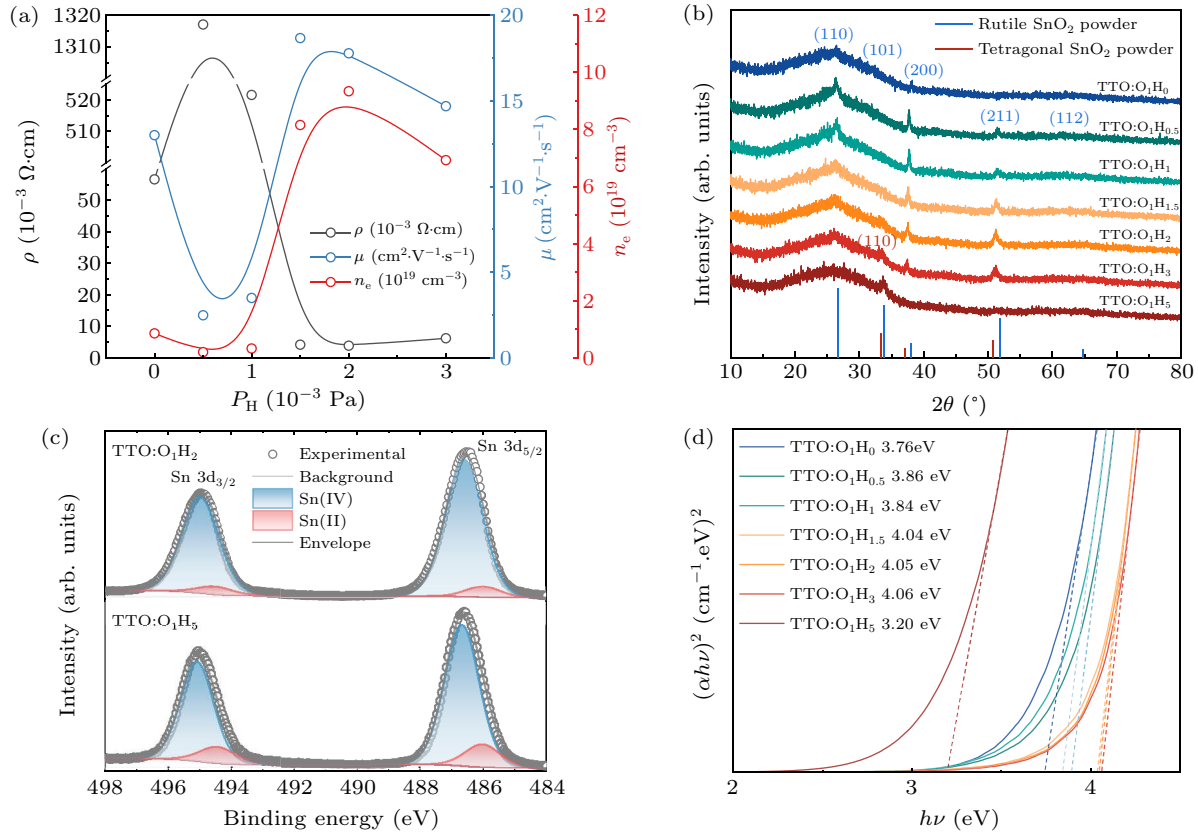


Fig. 3. Optoelectrical properties, microstructure, and Sn content of TTO films deposited with constant oxygen partial pressure P_O and varying hydrogen partial pressure P_H. (a) TTO film resistivities (ρ) in black, mobilities (μ) in blue and carrier concentrations (n_e) in red obtained by Hall measurements with guidelines; (b) XRD patterns of TTO films; (c) Sn 3d XPS spectra measured after argon plasma sputtering to remove surface contaminants and (d) Tauc plot and optical energy band gap.

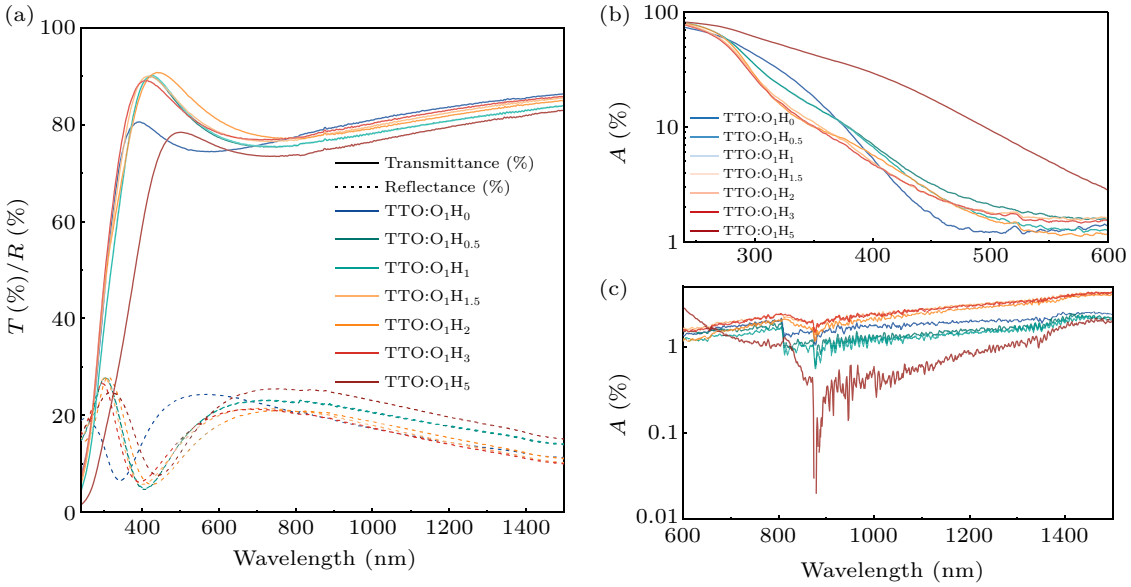


Fig. 4. Optical spectra of TTO films deposited with constant oxygen partial pressure P_O and varying hydrogen partial pressure P_H. (a) Optical transmittance (T) and reflectance (R) spectra of TTO films; (b) absorptance (A) spectra from short-wavelength range (240 nm–600 nm) and (c) long-wavelength range (600 nm–1500 nm).

To further analyze the optical properties of the TTO films, figure 4(a) presents the transmittance and reflectance spectra of TTO films, while Figs. 4(b) and 4(c) detail the absorption characteristics in the short-wavelength and near-infrared regions, respectively. In the short-wavelength range (< 600 nm), TTO films grown with hydrogen have lower optical absorption compared to those deposited in $Ar + O_2$ atmosphere, which could be explained by the relaxation of the defective pair Sn_i–V_O[31] due to the introduction of hydrogen in the ambient. For the long-wavelength region, optical absorption is affected by the high carrier concentration of the thin film, i.e., TTO:O_1H_y ($y = 1.5$, 2, 3) with high carrier concentration resulting in high free-carrier absorption. With the addition of an appropriate amount of hydrogen, the electrical properties of TTO can be optimized, achieving a balanced optoelectrical performance. For TTO film with excessive hydrogen, $y = 5$, short-wavelength absorptance increases intensively while free-carrier absorption at long wavelength is limited, indicating numerous deep-level defects and a great reduction in carrier concentration. The fit of Sn 3d XPS spectra in Fig. 3(c) shows that Sn(II) content in TTO:O_1H_5 becomes rich resulting from the reductive growth ambient. With the gathering of the isolated Sn(II) in SnO_2 lattice, even SnO grains are formed in the film. As a result, TTO:O_1H_5 shows severe absorption in the short-wavelength region.

4. Summary

This study systematically investigates the growth atmosphere effects on TTO film properties through controlled hydrogen and/or oxygen introduction into argon sputtering environments. Experimental results reveal that exclusive oxygen introduction forms amorphous SnO_2 phase with high resistivity, yet maintains low optical absorption (average 1.9%). On the other hand, hydrogen enhances reducibility to increase Sn(II) content, which deteriorates optical properties through SnO grain formation and isolated Sn(II)-induced short-wavelength absorption. The developed collaboration of H_2 and O_2 enables precise Sn(II) ratio and crystallinity control, achieving optimized TTO films with remarkably low resistivity (3.8×10^{-3} Ω·cm), high carrier concentration (9.3×10^{19} cm^{-3}) and mobility (17.8 $cm^2 \cdot V^{-1} \cdot s^{-1}$). At the same time, the film has exceptional optical characteristics. Its average transmittance is as high as 80.6% with a low average absorption of 1.9%. This cost-effective methodology demonstrates exceptional optoelectronic balance, showing great potential for solar cell and optoelectronic applications.

Acknowledgments

Project supported by the Key-Area Research and Development Program of Guangdong Province, China (Grant No. 2021B0101260001) and the Guangdong Basic and Applied Basic Research Foundation (Grant No. 2019A1515110411).

References

[1] De Wolf S, Descoeudres A, Holman Z C and Ballif C 2012 *High-efficiency Silicon Heterojunction Solar Cells: A Review Green* **2** 7
[2] Ellmer K 2012 *Nat. Photon.* **6** 809
[3] Li M, Mo C, Ji P, Zhang X, Chen J, Zhuge L, Wu X, Tan H and Huang T 2024 *Chin. Phys. B* **33** 108102
[4] Kostlin H, Jost R and Lems W 1975 *Phys. Stat. Sol. (a)* **29** 87
[5] Yao J K and Zhong W S 2023 *Chin. Phys. B* **32** 018101
[6] Ellmer K, Klein A and Rech B 2008 *Transparent Conductive Zinc Oxide: Basics and Applications in Thin Film Solar Cells* Vol. 104 (Berlin, Heidelberg: Springer Berlin Heidelberg)
[7] Yu C, Gao K, Peng C W, *et al.* 2023 *Nat. Energy* **8** 1375
[8] Batzill M and Diebold U 2005 *Progress in Surface Science* **79** 47
[9] Yu C, Gao K, Peng C W, *et al.* 2023 *Nat Energy* **8** 1375
[10] Wang X, Faizan M, Zhou K, Wang X, Fu Y and Zhang L 2024 *Chin. Phys. B* **33** 107303
[11] Swallow J E N, Williamson B A D, Whittles T J, Birkett M, Featherstone T J, Peng N, Abbott A, Farnworth M, Cheetham K J, Warren P, Scanlon D O, Dhanak V R and Veal T D 2018 *Adv. Funct. Mater.* **28** 1701900
[12] Williamson B A D, Featherstone T J, Sathasivam S S, Swallow J E N, Shiel H, Jones L A H, Smiles M J, Regoutz A, Lee T L, Xia X, Blackman C, Thakur P K, Carmalt C J, Parkin I P, Veal T D and Scanlon D O 2020 *Chem. Mater.* **32** 1964
[13] So H S, Park J W, Jung D H, Ko K H and Lee H 2015 *J. Appl. Phys.* **118** 085303
[14] Al-Kuhaili M F 2021 *Materials Chemistry and Physics* **257** 123749
[15] Fukumoto M, Nakao S, Shigematsu K, Ogawa D, Morikawa K, Hirose Y and Hasegawa T 2020 *Sci. Rep.* **10** 6844
[16] Uwihoreye V, Yang Z, Zhang J Y, Lin Y M, Liang X, Yang L and Zhang K H L 2023 *Sci. China Mater.* **66** 264
[17] Weidner M, Jia J, Shigesato Y and Klein A 2016 *Physica Status Solidi (b)* **253** 923
[18] Morán-Pedroso M, Sánchez-Marcos J, de Andrés A and Prieto C 2018 *Applied Surface Science* **459** 349
[19] Wu F, Tong X, Zhao Z, Gao J, Zhou Y and Kelly P 2017 *J. Alloys Compd.* **695** 765
[20] Holleman A F, Wiberg E, Wiberg N, Eagleson M, Brewer W and Aylett B J 2001 *Holleman-Wiberg Inorganic Chemistry* (London: Academic) pp. 900–911
[21] Singh A K, Janotti A, Scheffler M and Van De Walle C G 2008 *Phys. Rev. Lett.* **101** 055502
[22] Liu L Z, Xu J Q, Wu X L, Li T H, Shen J C and Chu P K 2013 *Appl. Phys. Lett.* **102** 031916
[23] Singh A V, Mehra R M, Yoshida A and Wakahara A 2004 *J. Appl. Phys.* **95** 3640
[24] Galazka Z, Uecker R, Klimm D, Irmscher K, Pietsch M, Schewski R, Albrecht M, Kwasniewski A, Ganschow S, Schulz D, Guguschev C, Bertram R, Bickermann M and Fornari R 2014 *Physica Status Solidi (a)* **211** 66
[25] Trani F, Causà M, Ninno D, Cantele G and Barone V 2008 *Phys. Rev. B* **77** 245410
[26] Luo H, Liang L Y, Cao H T, Liu Z M and Zhuge F 2012 *ACS Appl. Mater. Interfaces* **4** 5673
[27] Szuber J, Czempik G, Larciprete R, Koziej D and Adamowicz B 2001 *Thin Solid Films* **391** 198
[28] Weidner M, Brötz J and Klein A 2014 *Thin Solid Films* **555** 173
[29] Nakao S, Yamada N, Hitosugi T, Hirose Y, Shimada T and Hasegawa T 2010 *Thin Solid Films* **518** 3093
[30] Geurts J, Rau S, Richter W and Schmitte F J 1984 *Thin Solid Films* **121** 217
[31] Kılıç Ç and Zunger A 2002 *Phys. Rev. Lett.* **88** 095501